



Cite this: *Chem. Commun.*, 2023, 59, 9968

Received 29th May 2023,
Accepted 20th July 2023

DOI: 10.1039/d3cc02586a

rsc.li/chemcomm

Hybrid polymer dot-magnetic nanoparticle based immunoassay for dual-mode multiplexed detection of two mycotoxins[†]

Yi-Chen Chen,^{‡,a} Yu-Han Syu,^{‡,a} Jhen-Yan Huang,^a Chun-Yi Lin^a and Yang-Hsiang Chan^{ID, *abc}

We designed polymer dot-magnetic nanoparticle nanohybrids for signal enhancement in a test strip platform. Besides, the multicolor emissions of the Pdots embed multiplexing ability for this test strip. Two mycotoxins, aflatoxin B1 and zearalenone, were tested with the determined limits of detection of 2.15 ng mL^{-1} and 4.87 ng mL^{-1} , respectively.

Since the global pandemic of COVID-19 in recent years, there is no doubt that immunochromatography test strips (ICTS), the most widely used assay of point-of-care (POC) diagnostics, have become a prerequisite for daily testing to slow down disease transmission and thus reduce the number of hospitalizations. The incentive for the widespread use of ICTS lies in many aspects, including prompt result interpretation, large-scale testing, low cost, easy use, *etc.*^{1–5} Therefore, ICTS have been adopted in detecting diverse targets.^{6–14}

Though powerful, traditionally commercial ICTS possess several challenges, such as lower sensitivity and poorer specificity than standard laboratory facilities.^{4,15} Aiming at the improvement of the sensitivity and specificity of ICTS, recently, assay optimization and signal amplification strategies have been applied to ameliorate the assay kinetics and enhance the probe signals.^{16,17} Unfortunately, these techniques often lead to the issues of lengthening the assay test time^{18,19} and/or reducing detection specificity.^{20,21} To address this dilemma, a platform which can integrate assay optimization and signal amplification to achieve both higher sensitivity and specificity is highly desired. Herein, we integrated highly fluorescent polymer dots

(Pdots) with Fe_3O_4 magnetic nanoparticles (MNPs) as the reporter to achieve a dual-mode immunoassay. The ultrahigh fluorescence of the Pdots^{22–40} can greatly enhance the detection sensitivity of ICTS.^{21,41–43} However, we found that the high sensitivity due to signal amplification was also accompanied by an unwanted increase in false positives. This drive inspired us to create test strip platforms that are both sensitive and selective, while retaining the multiplexing capability of Pdots. Here, we endowed Pdots with magnetic properties by encapsulating MNPs inside the Pdots to form Pdot-MNP nanohybrids. It is important to note that numerous MNP-based test strip platforms have been developed, primarily employing MNPs for sample preconcentration purposes,⁴ but it is relatively uncommon to directly utilize the magnetic signal as a reporter for quantitative measurements of the targeted analytes.

In addition, the multi-color property of Pdots provides the chance to develop multiplexed ICTS for simultaneously detecting multiple analytes. Here, we selected two mycotoxins, aflatoxin B₁ (AFB₁) and zearalenone (ZEN), as the proof-of-concept targets. Mycotoxins are secondary metabolites with low molecular weight produced by filamentous fungi, including species such as *Aspergillus*, *Penicillium*, and *Fusarium*. AFB₁ is the predominant mycotoxin of *Aspergillus* and classified by the International Agency for Research on Cancer as a group I carcinogen.⁴⁴ ZEN, an estrogenic metabolite mainly produced by *Fusarium*, has a significant reproductive toxicity and teratogenic effects on humans.⁴⁵ Both AFB₁ and ZEN are common contaminants in cereal grains, nuts, and complete feeds such as rice, maize, wheat, corn, and peanuts. Therefore, the maximum levels and tolerance limits for AFB₁ and ZEN in food have been strictly regulated by many countries.^{46,47} For example, in the European Union, the maximum AFB₁ tolerance levels are 5 ppb and 2 ppb for nuts and cereals, respectively.⁴⁶ In Taiwan, the maximum tolerance levels are 12 ppb and 400 ppb for AFB₁ and ZEN, respectively.⁴⁸ The performance of the detection for AFB₁ and ZEN using Pdot-MNP-based ICTS is elaborated as follows.

To endow fluorescent Pdots with magnetic properties, we integrated Pdots with MNPs by electrostatic interactions

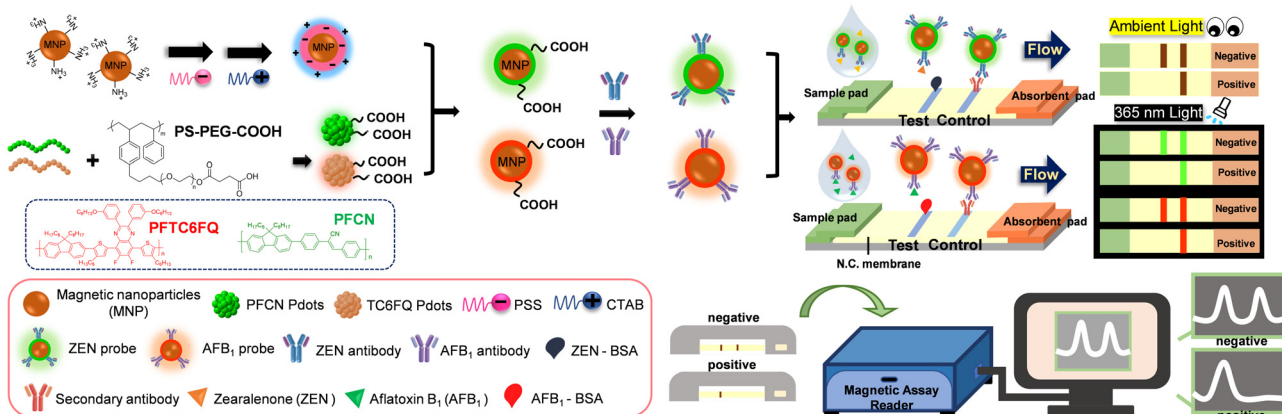
^a Department of Applied Chemistry, National Yang Ming Chiao Tung University, Hsinchu, 30010, Taiwan. E-mail: yhchan@nycu.edu.tw

^b Center for Emergent Functional Matter Science, National Yang Ming Chiao Tung University, Hsinchu, 30010, Taiwan

^c Department of Medicinal and Applied Chemistry, Kaohsiung Medical University, Kaohsiung, 80708, Taiwan

[†] Electronic supplementary information (ESI) available: Video of testing the real samples, synthesis of the polymers, and Fig. S1–S7. See DOI: <https://doi.org/10.1039/d3cc02586a>

[‡] Both authors contributed equally to this work.



Scheme 1 Schematic showing the approach used by a MNP@Pdot-based lateral flow test strip for detection of mycotoxins.

(Scheme 1, see ESI[†] for detailed discussions). Fig. S1A (ESI[†]) showcases the optical properties of different materials, including bare MNPs (dashed brown line), MNP@PFCN (dashed/solid green line), and MNP@PFTC6FQ (dashed/solid red lines). Before coating with Pdots, the MNPs showed strong absorption below 400 nm and no fluorescence in the visible region. After coating with Pdots, representative absorption and emission peaks of Pdots clearly appeared. The rationale behind the selection of PFCN Pdots with green emission and PFTC6FQ Pdots with orange-red fluorescence was based on the noticeable difference in color between the two under 365 nm excitation. When the two fluorescence colors are mixed, it leads to a conspicuous color transition from the original colors, which is advantageous for facilitating multiplexing detection. In Fig. S1B (ESI[†]), the TEM image shows the MNPs before the Pdot coating process. The MNPs exhibit an average hydrodynamic diameter of 10 nm, as determined through dynamic light scattering (DLS) measurements. The TEM images of MNPs subsequent to the encapsulation of PFCN and PFTC6FQ Pdots are depicted in Fig. S1C and D (ESI[†]), respectively. Furthermore, the hydrodynamic sizes of the MNP@PFCN and MNP@PFTC6FQ nano-hybrids increased to 48 nm and 54 nm, respectively. The above results, which encompass zeta potential measurements, optical characterization, TEM imaging, and DLS data, confirm the successful surface modification of MNPs with Pdots.

The as-prepared MNP@PFCN nanoparticles were then conjugated with ZEN antibodies, while MNP@PFTC6FQ nanorods were decorated with AFB₁ antibodies. Following conjugation, the MNP@Pdot nano-hybrids exhibit dual capabilities of magnetic/fluorescent readout and targeted recognition. Scheme 1 shows the production of a nitrocellulose membrane comprising a control line and a test line. As there were no commercially available paired ZEN/AFB₁ antibodies, a competitive immunoassay was utilized. Consequently, the control line was equipped with IgG secondary antibodies, whereas the test line was customized to include ZEN-BSA, AFB₁-BSA, or a combination of both for multiplexed detection. It is important to note that the direct use of bare ZEN or AFB₁ antigens is not viable due to their low affinity with the nitrocellulose membrane. A

plastic case was used to assemble and accommodate each set of test strips, which consisted of a sample pad, a nitrocellulose membrane, and an absorbent pad. After the analytes and MNP@Pdot probes were added to the sample well of the test strip, the running buffer was introduced. The capillary action facilitated the movement of analytes and probes across the test strip, transferring them from the sample pad to the absorbent pad. The running buffer acted as a carrier for the analytes and probes, facilitating their movement through the test strip. The MNP@Pdot probes interacted with the analytes during their journey, allowing for the detection and quantification of the target analytes. Overall, this process enabled the efficient and effective detection of the analytes of interest. If ZEN is absent in the sample, the MNP@PFCN hybrids will attach to the ZEN antigens on the test line, resulting in the immediate visualization of green fluorescence from PFCN under UV irradiation. On the contrary, If ZEN is present in the sample, no green fluorescence from PFCN will be visible on the test line. This method is ideal for fast qualitative identification. The same mechanism also applies to MNP@PFTC6FQ in detecting AFB₁. The magnetic intensity ratios of the test line to the control line (T/C) can be utilized for quantitative measurements in both cases, owing to the minimal magnetic signal background interference in food. We expect that this bimodal signal readout ICTS, which combines fluorescent and magnetic properties, will be an effective tool for diagnosing mycotoxins in food.

To begin the assessment, the specificity of MNP@PFCN and MNP@PFTC6FQ nanoprobe for ZEN and AFB₁, respectively, was examined. According to Fig. 1A and B, the MNP@PFCN probes exhibited a notable specificity towards ZEN, with negligible non-specific binding observed for other antigens such as AFB₁, ochratoxin A (OTA), and deoxynivalenol (DON). The ability of fluorescence to distinguish signals was found to be even better than the color depth from MNPs in Fig. 1A, as evidenced by the highly distinguishable fluorescence signals of Pdots in Fig. 1B. This highlights the excellent qualitative performance of fluorescence. In a similar fashion, MNP@PFTC6FQ nano-hybrids demonstrated high specificity towards AFB₁, as shown in Fig. 1C and D. It is worth noting that we

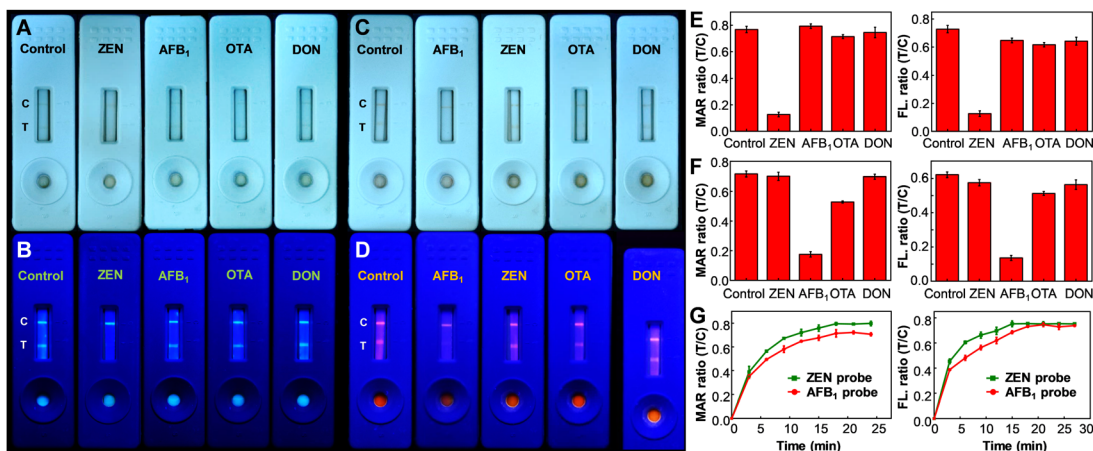


Fig. 1 Selectivity performance of MNP@PFCN and MNP@PFTC6FQ probes on different mycotoxins. (A) Photographs of the test strips employing MNP@PFCN probes under ambient lighting conditions, and (B) their respective fluorescent images upon excitation with 365 nm light after reacting with analytes containing distinct antigens (150 ng mL⁻¹ for ZEN, AFB₁, and OTA; 750 ng mL⁻¹ for DON). (C) The test strips were photographed using MNP@PFTC6FQ probes in ambient light, while (D) their corresponding fluorescent images were captured under 365 nm light excitation after reacting with analytes that contained various antigens (ZEN, AFB₁, and OTA at 150 ng mL⁻¹; DON at 750 ng mL⁻¹). (E) Magnetic intensity ratios (left panel) and fluorescence ratio (right panel) of T/C measured in (A) and (B), respectively. (F) Magnetic intensity ratios (left panel) and fluorescence ratios (right panel) of T/C measured in (C) and (D), respectively. (G) Magnetic intensity ratios (left panel) and fluorescence ratios (right panel) of the T/C measured at different reaction times for the ZEN detection using MNP@PFCN probes and AFB₁ detection using MNP@PFTC6FQ probes. Each dataset was subjected to at least three repeated measurements.

observed a magnetic intensity ratio of T/C that was more than five times higher for MNP@PFCN towards ZEN than towards other reagents (as shown in the left panel of Fig. 1E). In contrast, the fluorescence intensity ratio of T/C for MNP@PFCN towards ZEN was about four times higher than towards other reagents (as depicted in the right panel of Fig. 1E). This indicates that the detection sensitivity based on magnetic signals is higher than that based on fluorescence signals. The same trend is observed in the case of MNP@PFTC6FQ probes, as depicted in Fig. 1F. The superior sensitivity of magnetic signals compared to fluorescence signals can be attributed to the minimal magnetic background from food and nitrocellulose membranes. This leads to higher signal-to-noise ratios and enables more accurate and reliable quantitative detection. The above results suggest that the fluorescence intensities are ideal for qualitative screening purposes, while magnetic signals are more appropriate for precise quantitative measurements. According to the aforementioned findings, the bimodal readout ICTS platform exhibits exceptional specificity for detecting ZEN or AFB₁, with minimal occurrences of false negatives and false positives. Fig. 1G illustrates the monitoring of magnetic and fluorescence signals from the test and control lines at varying reaction times, which is a crucial aspect for a competent ICTS platform to rapidly acquire test results. It can be inferred that a reaction time of 20 min is adequate for both probes to decipher the testing results. In addition to specificity, the sensitivity of detection is equally important to assess the performance of these new probes (see ESI[†] and Fig. S4). Using magnetic signals, the detection linearity of ZEN with MNP@PFCN ranged from 0 to 100 ng mL⁻¹, which is suitable for the maximum tolerance level of ZEN (400 ng mL⁻¹) regulated in Taiwan, taking into account the sample pretreatment process that requires a

dilution of 4–10 times. MNP@PFTC6FQ probes also exhibited a good dynamic range from 0 to 25 ng mL⁻¹ for AFB₁ (Fig. S4E and F, ESI[†]). The limit of detection for ZEN and AFB₁ was determined to be 4.87 ng mL⁻¹ and 2.15 ng mL⁻¹, respectively.^{49–52} The practicability of this MNP@Pdot-based ICTS platform in real samples was also evaluated in this work (see ESI[†] Fig. S5).

The multiplexing detection ability can be imparted to Pdots through their ability to emit multiple colors and absorb a wide range of spectra. Fig. 2A illustrates the construction of the test strip, in which a blend of antigens of ZEN and AFB₁ was utilized to modify the test line. Conceptually, magnetic signals can be utilized to quantify the overall quantity of ZEN and AFB₁, whereas fluorescence color is well-suited for discriminating between ZEN and AFB₁. The performance of the multiplexed sensing capability was depicted in Fig. 2B and C. The negative control sample (lacking ZEN and AFB₁) displayed a visible test line to the naked eye, emitting a distinct white-yellow emission light, manifesting the occurrence of minimal false-positive effects on this platform. When only AFB₁ was present, a faintly discernible test line was observed by the naked eye, accompanied by green fluorescence. In the presence of only ZEN, a barely noticeable test line was observed by the naked eye, accompanied by orange fluorescence. In the case of the presence of both ZEN and AFB₁, a test line cannot be detected visually and emissions are barely noticeable. It is noteworthy that the control line displayed a yellow-white fluorescence color, which was produced by the merging of green (PFCN) and red (PFTC6FQ) fluorescence. The magnetic quantitation data presented in Fig. 2D support the findings mentioned above; however, it is not possible to differentiate the presence of either ZEN or AFB₁ alone. The findings indicate that the bimodal MNP@Pdot-based ICTS platform is highly dependable

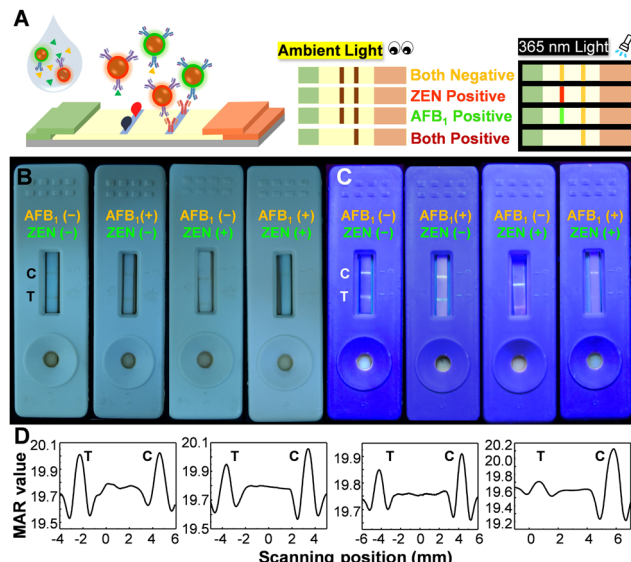


Fig. 2 (A) A diagram illustrating the production process of multiplexed ICTS for co-detection of ZEN and AFB₁. (B) Photographs of test strips after interacting with sample solutions containing varying concentrations of AFB₁ and ZEN. Their corresponding (C) fluorescence images under UV light and (D) magnetic signals. The AFB₁/ZEN concentrations in (B–D) are as follows (from left to right): 0/0, 150/0, 0/150, 150/150 ng mL⁻¹.

and has low cross-interference, making it suitable for the simultaneous detection of ZEN and AFB₁ in mixed mycotoxin samples.

We have devised a bimodal ICTS platform based on MNP@Pdot for the qualitative and quantitative diagnosis of ZEN and AFB₁ in food. The test can be performed on-site and interpreted within 20 minutes. This ICTS has the potential for multiplexed detection of both ZEN and AFB₁ at the same time, ensuring food safety by detecting their levels. Furthermore, the detection limit of this ICTS system is low enough to conform to the maximum tolerance levels of ZEN (400 ng mL⁻¹) and AFB₁ (12 ng mL⁻¹) regulated in Taiwan. We expect that this user-friendly yet powerful ICTS will have widespread utility in quickly screening for ZEN and AFB₁ in food.

Conflicts of interest

There are no conflicts to declare.

Notes and references

1. J. Budd, *Nat. Rev. Bioeng.*, 2023, **1**, 13–31.
2. X. Gong, *et al.*, *J. Mater. Chem. B*, 2017, **5**, 5079–5091.
3. A. Sena-Torralba, R. Álvarez-Diduk, C. Parolo, A. Piper and A. Merkoci, *Chem. Rev.*, 2022, **122**, 14881–14910.
4. Y. Liu, L. Zhan, Z. Qin, J. Sackrison and J. C. Bischof, *ACS Nano*, 2021, **15**, 3593–3611.

5. S. Nayak, N. R. Blumenfeld, T. Laksanasopin and S. K. Sia, *Anal. Chem.*, 2017, **89**, 102–123.
6. Y.-T. Tsao, *et al.*, *Trends Mol. Med.*, 2020, **26**, 1118–1132.
7. Y. Wu, *et al.*, *Biosens. Bioelectron.*, 2020, **157**, 112168.
8. L. Liu, D. Yang and G. Liu, *Biosens. Bioelectron.*, 2019, **136**, 60–75.
9. T. Mahmoudi, M. D. L. Guardia and B. Baradaran, *Trends Anal. Chem.*, 2020, **125**, 115842.
10. A. Jones, L. Dhanapala, R. N. T. Kankanamage, C. V. Kumar and J. F. Rusling, *Anal. Chem.*, 2020, **92**, 345–362.
11. T. Mahmoudi, M. D. L. Guardia, B. Shirdel, A. Mokhtarzadeh and B. Baradaran, *Trends Anal. Chem.*, 2019, **116**, 13–30.
12. V.-T. Nguyen, S. Song, S. Park and C. Joo, *Biosens. Bioelectron.*, 2020, **152**, 112015.
13. J. Wang, *et al.*, *Angew. Chem., Int. Ed.*, 2021, **60**, 13042–13049.
14. Y.-H. Chen, *et al.*, *Anal. Chem.*, 2021, **93**, 5556–5561.
15. B. Udagama, *et al.*, *ACS Nano*, 2020, **14**, 3822–3835.
16. T. Liang, *et al.*, *Anal. Chem.*, 2016, **88**, 2311–2320.
17. X. He, *et al.*, *ACS Sens.*, 2019, **4**, 1691–1700.
18. J. D. Bishop, H. V. Hsieh, D. J. Gasperino and B. H. Weigl, *Lab Chip*, 2019, **19**, 2486–2499.
19. T.-T. Tsai, *et al.*, *Sci. Rep.*, 2018, **8**, 17319.
20. L. Zhan, *et al.*, *Microsyst. Nanoeng.*, 2020, **6**, 54.
21. Y.-Q. Yang, Y.-C. Yang, M.-H. Liu and Y.-H. Chan, *Anal. Chem.*, 2020, **92**, 1493–1501.
22. K. Pu, *et al.*, *Nat. Nanotechnol.*, 2014, **9**, 233–239.
23. K. Pu, N. Chattopadhyay and J. Rao, *J. Controlled Release*, 2016, **240**, 312.
24. X. Lim, *Nature*, 2016, **531**, 26–28.
25. C. Wu, B. Bull, C. Szymanski, K. Christensen and J. McNeill, *ACS Nano*, 2008, **2**, 2415–2423.
26. C. Wu, *et al.*, *Angew. Chem., Int. Ed.*, 2011, **50**, 3430–3434.
27. Y.-H. Chan and P.-J. Wu, *Part. Part. Syst. Charact.*, 2015, **32**, 11–28.
28. S. Li, *et al.*, *Chem. Mater.*, 2016, **28**, 8669–8675.
29. Y. Lyu, C. Xie, S. A. Chechetka, E. Miyako and K. Pu, *J. Am. Chem. Soc.*, 2016, **138**, 9049–9052.
30. H.-Y. Liu, *et al.*, *J. Am. Chem. Soc.*, 2015, **137**, 10420–10429.
31. C.-S. Ke, *et al.*, *ACS Nano*, 2017, **11**, 3166–3177.
32. L. Feng, *et al.*, *Chem. Soc. Rev.*, 2013, **42**, 6620–6633.
33. Y. Lyu, X. Zhen, Y. Miao and K. Pu, *ACS Nano*, 2017, **11**, 358–367.
34. Y. Lyu, *et al.*, *ACS Nano*, 2016, **10**, 4472.
35. K. Sun, *et al.*, *ACS Nano*, 2016, **10**, 6769–6781.
36. X. Chen, *et al.*, *Adv. Mater.*, 2017, **29**, 1604859.
37. W. K. Tsai and Y. H. Chan, *J. Chin. Chem. Soc.*, 2019, **66**, 9–20.
38. Y. Jiang and K. Pu, *Acc. Chem. Res.*, 2018, **51**, 1840–1849.
39. X. Zhen, C. Xie and K. Pu, *Angew. Chem., Int. Ed.*, 2018, **57**, 3938–3942.
40. Y. Jiang and J. McNeill, *Chem. Rev.*, 2017, **117**, 838–859.
41. C.-C. Fang, *et al.*, *Anal. Chem.*, 2018, **90**, 2134–2140.
42. P.-Y. You, F.-C. Li, M.-H. Liu and Y.-H. Chan, *ACS Appl. Mater. Interfaces*, 2019, **11**, 9841–9849.
43. Y.-C. Yang, M.-H. Liu, S.-M. Yang and Y.-H. Chan, *ACS Sens.*, 2021, **6**, 4255–4264.
44. World Health Organization, International agency for research on cancer. <https://monographs.iarc.who.int/agents-classified-by-the-iarc/> (accessed May 27, 2023).
45. J. W. Bennett and M. Klich, *Clin. Microbiol. Rev.*, 2003, **16**, 497–516.
46. L. Wu, *et al.*, *J. Anim. Sci. Biotechnol.*, 2016, **7**, 63.
47. Economic Research Service, United States Department of Agriculture. https://www.ers.usda.gov/webdocs/publications/41603/15640_aer828h_1_.pdf?v=0 (accessed May 27, 2023).
48. Taiwan Food and Drug Administration. <https://consumer.fda.gov.tw/Law/Detail.aspx?nodeID=518&lawID=741> (accessed May 27, 2023).
49. D. Zhu, L. Xue, G. Li, Y. Che and H. Jiang, *Org. Chem. Front.*, 2014, **1**, 501–505.
50. P. Alam, *et al.*, *Chem. Eur. J.*, 2017, **23**, 14911–14917.
51. F. M. d R. Lima, *et al.*, *Microchim. Acta*, 2018, **185**, 521.
52. X. Pei, *et al.*, *Anal. Chem.*, 2014, **86**, 4893–4900.